



## Facet effect of $\text{Co}_3\text{O}_4$ nanocrystals on visible-light driven water oxidation

Xichen Zhou<sup>a</sup>, Zhen Liu<sup>a</sup>, Yifan Wang<sup>a</sup>, Yong Ding<sup>a,b,\*</sup>



<sup>a</sup> State Key Laboratory of Applied Organic Chemistry, Key Laboratory of Nonferrous Metal Chemistry and Resources Utilization of Gansu Province and College of Chemistry and Chemical Engineering, Lanzhou University, Lanzhou 730000, China

<sup>b</sup> State Key Laboratory of Rare Earth Resource Utilization Changchun Institute of Applied Chemistry, Chinese Academy of Sciences, Changchun 130022, China

### ARTICLE INFO

**Keywords:**  
Photocatalysis  
Water oxidation  
Oxygen evolution  
 $\text{Co}_3\text{O}_4$   
Facet effect

### ABSTRACT

The deep comprehension of water oxidation mechanisms and structure-activity relationships on heterogeneous catalysts remains challenging. Here, facet effect of model spinel  $\text{Co}_3\text{O}_4$  on water oxidation driven by visible-light is investigated in a well-established  $[\text{Ru}(\text{bpy})_3]^{2+}-\text{S}_2\text{O}_8^{2-}$  ( $\text{bpy} = 2,2\text{-bipyridine}$ ) biomimetic system to unveil the internal water oxidation mechanism for the first time. Spinel  $\text{Co}_3\text{O}_4$  catalysts in the morphologies of nanocube, nanorod and nanosheet are synthesized successfully by bottom-up nanotechnologies, and they predominantly expose the well-defined crystal planes of {100}, {110} and {112}, respectively. Using time-resolved laser flash photolysis approach, the dynamically electronic transfer in photocatalytic courses of three  $\text{Co}_3\text{O}_4$  catalysts are distinguished in the nanosecond scale. The three model catalysts show a facet-dependent activity rule that the water oxidation performance of {112} is similar with that of {110} and much better than that of {100}. The  $\text{Co}^{2+}$ - $\text{Co}^{2+}$  active sites with an ionic distance of 3.495 Å for catalyzing water oxidation only appear in {112} and {110} planes except for {100}, which is possibly responsible for the unique activity order of three  $\text{Co}_3\text{O}_4$  catalysts. Furthermore, the  $\text{Co}^{2+}$  ions in the tetrahedral sites of spinel  $\text{Co}_3\text{O}_4$  are confirmed to be more active than the  $\text{Co}^{3+}$  ions in the octahedral sites under visible-light driven water oxidation. The new insights shed a light on developing advanced nanocatalysts for oxygen evolution reaction.

### 1. Introduction

Water splitting driven by artificial photosynthetic system provides a sustainable and environment friendly development blueprint for mankind to address energy and environmental crisis through producing oxygen and carbon-neutral hydrogen [1,2]. As the rate-determining half-reaction of water splitting, water oxidation ( $2\text{H}_2\text{O} \rightarrow \text{O}_2 + 4\text{H}^+ + 4\text{e}^-$ , oxygen evolution reaction, OER) always involves a thermodynamically uphill four-electron transfer, resulting in sluggish kinetics and thus needing high-activity catalysts to reduce the reaction energy barrier [3–5].

Since heterogeneous catalysis of water oxidation is of essential importance to the generation of solar fuel on a global scale, the investigation on the catalytic reaction mechanism using model heterogeneous catalysts is crucial and urgently needed [6–9]. As typical surface and interface processes, in the course of heterogeneous water oxidation, water or hydroxy is firstly adsorbed and activated on specific sites of catalyst surface, and then the proton-coupled electron transfer (PCET) processes occur accompanied by the formation of a series of intermediates of oxygen species [10]. These intermediates are

chemically transformed to form the  $\text{O}-\text{O}$  bonds, then the  $\text{O}_2$  will be released [11]. Compared with the bulk structure of catalysts, the reaction paths of heterogeneous catalysis depend largely on the different surface states of catalysts. Variation in arrangement patterns of surface atoms, geometrical and electronic structures of different crystal planes can cause distinctive selectivity and activity of heterogeneous catalysts [12,13]. Nowadays, rapidly developing nanotechnologies enable us to synthesize model catalysts with well-defined shapes and facets to investigate catalytic reaction mechanism [14]. Employing bottom-up chemistry approaches, shape and crystal plane effects have been discovered and studied in catalysis on the platform of noble metals (for example, Pt, Pd, Rh, Au and Ag), noble metal alloys (for example, Pt-Pd, Pt-Rh and Pt-Ni) and metal oxides (for example,  $\text{CeO}_2$ ,  $\text{CuO}$  and  $\text{Fe}_3\text{O}_4$ ) [13,15].

As one of the best single metal oxide catalysts for water oxidation, spinel  $\text{Co}_3\text{O}_4$  comprises of two kinds of cobalt ions, namely  $\text{Co}^{2+}$  in a tetrahedral coordination and  $\text{Co}^{3+}$  in an octahedral coordination [16]. Thereinto, the  $\text{Co}_4\text{O}_4$  cubane motif consisting of  $\text{Co}^{3+}$  and  $\text{O}^{2-}$  combining with  $\text{Co}^{2+}$  exhibits a similar construction with the natural water oxidation catalyst (WOC) in PSII ( $\text{Mn}_4\text{CaO}_5$ ) of green plants,

\* Corresponding author at: State Key Laboratory of Applied Organic Chemistry, Key Laboratory of Nonferrous Metal Chemistry and Resources Utilization of Gansu Province and College of Chemistry and Chemical Engineering, Lanzhou University, Lanzhou 730000, China.

E-mail addresses: [dingyong1@lzu.edu.cn](mailto:dingyong1@lzu.edu.cn), [dingyong1973@163.com](mailto:dingyong1973@163.com) (Y. Ding).

cyanobacteria, and algae [17–19]. Investigating the photocatalytic water oxidation mechanism towards  $\text{Co}_3\text{O}_4$  not only gives us a deeper insight to the natural photosynthesis, but also accelerates the course of exploiting high-performance artificial WOCs. Previous studies on shape-controlled  $\text{Co}_3\text{O}_4$  (for example, catalyzing oxidation of carbon monoxide, reduction of oxygen and combustion of methane) have revealed that their catalytic performance are closely related with their shapes as a result of well-defined crystal planes [12,14,20]. Compared and analyzed with the different catalytic behaviors of  $\text{Co}_3\text{O}_4$  model catalysts with different exposed facets, the catalytic mechanism can be recognized and understood on the atomic or ionic level. However, up to now, atomic-level comprehension on the role of the surface atoms of heterogeneous catalysts during photocatalytic water oxidation is still at infant stage. Rare studies focus on the crystal plane effects of  $\text{Co}_3\text{O}_4$  toward water oxidation, and detailed understanding of profoundly catalytic mechanism remains in great need [21,22], not to mention the influence upon different crystal facets of  $\text{Co}_3\text{O}_4$  under visible-light driven water oxidation system.

Herein, we employ the spinel  $\text{Co}_3\text{O}_4$  nanocubes, nanorods and nanosheets as model catalysts to build a bridge between the microcosmic crystal plane structure and the macroscopically catalytic activity, aiming to investigate the structure–activity relationship and water oxidation mechanism of  $\text{Co}_3\text{O}_4$  in a well-established  $[\text{Ru}(\text{bpy})_3]^{2+}$ – $\text{S}_2\text{O}_8^{2-}$  biomimetic protocol system driven by visible-light. Time-resolved laser flash photolysis experiments reveal the faster electron transfer from water to {112} and {110} crystal planes of  $\text{Co}_3\text{O}_4$  with high valence than that of {100} planes during photocatalytic water oxidation process. The  $\text{Co}^{2+}$ – $\text{Co}^{2+}$  active sites with an ionic distance of 3.495 Å are found only in {112} and {110} crystal planes instead of {100} planes, which may account for the better catalytic activity of {112} and {110} crystal planes. Moreover, we confirm that the  $\text{Co}^{2+}$  ions in spinel  $\text{Co}_3\text{O}_4$  are more active than  $\text{Co}^{3+}$  ions under visible-light driven water oxidation.

## 2. Experiment section

### 2.1. Material

All chemicals of analytical grade were used in the experiments directly without further purification. Purified water ( $18.2 \text{ M}\Omega \text{ cm}$ , TOC < 3 ppb) used for preparing solutions was produced by Molecular Lab Water Purifier.

### 2.2. Synthesis of $\text{Co}_3\text{O}_4$ nanorod

$\text{Co}_3\text{O}_4$  nanorods were synthesized according to the reported literature [14]. In a typical synthesis, dissolve 4.98 g of cobalt acetate tetrahydrate in 60 mL ethylene glycol at room temperature. Heat the mixture to 160 °C gradually. Add 200 mL 0.2 M  $\text{Na}_2\text{CO}_3$  aqueous solution to the mixture drop by drop till the pH value reach 10 under vigorous stirring with reflux of continuous argon flow. Age the slurry at 160 °C for 1 h under vigorous stirring with reflux of continuous argon flow. Filter the slurry at room temperature and wash the precipitate with hot water. Dry the solid at 50 °C overnight under vacuum. Finally, through an annealed process at 450 °C for 3 h,  $\text{Co}_3\text{O}_4$  nanorods were obtained.

### 2.3. Synthesis of $\text{Co}_3\text{O}_4$ nanocube

Nanocubes of the spinel  $\text{Co}_3\text{O}_4$  were synthesized by a nitrate-salt-mediated method reported by Feng and Zeng with some modifications [23]. In a typical process, 60.0 g  $\text{NaNO}_3$  was added into an aqueous solution of  $\text{NaOH}$  (100.0 mL, 0.3 M) in a three-necked round bottom flask under vigorous stir. This reaction mixture was kept at a temperature of 120 °C with a water-cooled reflux. Then,  $\text{Co}(\text{NO}_3)_2 \cdot 6\text{H}_2\text{O}$  (20.0 mL, 1.0 M) aqueous solution was added to the flask within 1 min

and an instantaneous precipitation can be obtained. Upon heating and bubbling with purified air ( $50 \text{ mL m}^{-1}$ ) for 12 h, the colour of the precipitate slowly changed from blue to brown and finally to black. The resulting black slurry was centrifuged at 8000 rpm. The solid obtained was washed several times with  $\text{HCl}$  (2.0 M), deionized water, and then vacuum dried at room temperature. After an annealed process at 450 °C for 3 h,  $\text{Co}_3\text{O}_4$  nanocubes were obtained.

### 2.4. Synthesis of $\text{Co}_3\text{O}_4$ nanosheet

$\text{Co}_3\text{O}_4$  nanosheets were synthesized according to a reported hydrothermal method with some modifications [24]. In a typical synthesis route, 0.52 g  $\text{Co}(\text{NO}_3)_2 \cdot 6\text{H}_2\text{O}$  was dissolved in 40 mL ultrapure water and then was mixed with hexamethylenetetramine aqueous solution (0.24 g HMTA, 40 mL) under continuous stirring. Few drops of  $\text{NaOH}$  aqueous solution (10 M) were added in the resultant solution gradually to adjust the pH to 10. After that, the resultant solution was vigorously stirred for 2 h. Subsequently, the resultant solution was loaded into a 100 mL Teflon-lined stainless steel autoclave, sealed and heated up to 110 °C for 15–24 h. After completing the reaction in desired time, the autoclave was naturally allowed to cool down at room-temperature. The obtained products were washed with DI water, ethanol and acetone sequentially and dried at room-temperature. The dried products were then calcined at 450 °C for 3 h to obtain  $\text{Co}_3\text{O}_4$  nanosheets.

### 2.5. Synthesis of $\text{ZnCo}_2\text{O}_4$

Spinel  $\text{ZnCo}_2\text{O}_4$  was synthesized with a low-temperature coprecipitation method [25]. In the course of synthesis, poly(ethylene oxide)–poly(propylene oxide)–poly(ethylene oxide) (P123, 1.00 g) and oxalic acid ( $\text{H}_2\text{C}_2\text{O}_4$ , 2.80 g) were totally dissolved in a mixed solution of ethanol (25 mL) and PEG (Mw = 200, 100 mL) with magnetic stirring. Later, 5 mL  $\text{Zn}(\text{NO}_3)_2 \cdot 6\text{H}_2\text{O}$  (0.5 M) and 10 mL  $\text{Co}(\text{NO}_3)_2 \cdot 6\text{H}_2\text{O}$  (0.5 M) were added into the above solution. The mixed solution was stirred for 30 min until the formation of the pink precipitate, which were collected by centrifugation later and washed with deionized water as well as absolute ethanol for several times. Whereafter, the precipitates were dried in air at 60 °C for 12 h. Finally, through an annealed process at 450 °C for 3 h,  $\text{ZnCo}_2\text{O}_4$  sample was obtained.

### 2.6. Synthesis of $\text{CoAl}_2\text{O}_4$

$\text{CoAl}_2\text{O}_4$  sample was synthesized by a sol-gel method [26]. In a typical synthesis, 3 mmol  $\text{Co}(\text{NO}_3)_2 \cdot 6\text{H}_2\text{O}$ , and 6 mmol  $\text{Al}(\text{NO}_3)_3 \cdot 9\text{H}_2\text{O}$  were mixed in 9 mL of 1.5 M citric acid solution at room temperature. Following, the resulting solution was openly heated and stirred at 80 °C for 3 h to obtain the sol, which would gradually convert into thick gel. The obtained gel was dried at 120 °C. After carefully milling the dry powder, the precursor was further calcined at 800 °C for 5 h to obtain spinel  $\text{AlCo}_2\text{O}_4$ .

### 2.7. Instruments

A X’Pert PRO diffractometer (Netherland) was employed to obtain the Powder X-ray diffraction (PXRD) data with a  $\text{Cu K}\alpha$  radiation ( $\lambda = 1.5418 \text{ \AA}$ ). X-ray photoelectron spectra (XPS) were used by ESCALAB250xi instrument with X-ray monochromatization. C 1s peak (284.8 eV) from residual carbon was conducted to correct the binding energy of other elements. Field emission scanning electron microscopy (FE-SEM) images were undertaken on a Hitachi S-4800 operated at a scanning voltage of 5.0 kV. Transmission electron microscopy (TEM), high resolution TEM (HRTEM) data were collected by a TecnaiG<sup>2</sup>F30 instrument. Specific surface areas were calculated from the  $\text{N}_2$  adsorption/desorption data obtained at 77 K (Micromeritics ASAP 2020 M system) using the BJH (Barrett–Joyner–Halenda) and BET methods. UV-vis absorption spectra were recorded on a TU-1810 spectro-

photometer (Beijing Purkinje General Instrument Co., Ltd.) equipped with a photomultiplier tube detector. Fluorescence spectra of  $[\text{Ru}(\text{bpy})_3]\text{Cl}_2$  solutions were collected on a F-7000 FL Spectrophotometer. Zeta potentials of  $\text{Co}_3\text{O}_4$  samples were carried out using a Zetasizer Nano 3600 instrument (Malvern Instruments Ltd.) in 100 mM borate buffer with 1 g  $\text{L}^{-1}$  catalysts. The pH of all solution was determined by a FiveEasyplus pH meter of Mettler-Toledo Instruments Ltd.

### 2.8. Photocatalytic water oxidation

Water oxidation experiments were performed in the well-established  $[\text{Ru}(\text{bpy})_3]^{2+} - \text{S}_2\text{O}_8^{2-}$  protocol system. A blue LED light source was used for reactions with wavelength of  $460 \pm 10 \text{ nm}$  and FWHM of  $15\text{--}20 \text{ nm}$ , and the luminous power was fixed at  $\sim 30 \text{ mW/cm}^2$ . Clark electrode (OX-NP, Unisense) was used to measure the produced dissolved oxygen in the solution. Before experiment, a 10 mL solution was prepared by mixing catalysts (0.3 g  $\text{L}^{-1}$ ),  $[\text{Ru}(\text{bpy})_3]\text{Cl}_2$  (1.0 mM) and  $\text{Na}_2\text{S}_2\text{O}_8$  (5.0 mM) in buffer solution at dark. Then, the oxygen in liquid phase was removed by bubbling Ar gas. After the oxygen in the solution was drained clean, the Ar gas was flowing above the liquid (in the headspace of vial) to prohibit the oxygen of air dissolve in the liquid again. For gas chromatography measurements, the solution was prepared as same as above. Then, the above solution was deaerated with Ar gas to remove  $\text{O}_2$  in both liquid phase (10 mL) and head space of vial (15.8 mL) for 15 min in a special flask sealed by a rubber plug. Next, the reactor was illuminated with the LED light source at room temperature. After each detecting interval, 100  $\mu\text{L}$  of Ar gas was pushed into the special flask and then same 100  $\mu\text{L}$  of the gas in the head space of the vial was taken with a SGE gas-tight syringe and determined by gas chromatography (GC) equipped with 5 Å molecular sieves and thermal conductivity detector (TCD). The entire amount of generated  $\text{O}_2$  was calculated by the concentration of  $\text{O}_2$  that dispersed in the headspace gas. Nanosecond transient absorption measurements were performed on an Edinburgh Instruments LP920-KS laser flash photolysis spectrometer, using an OPO laser source (OPOTEK Vibrant). Transient detection was obtained with a photomultiplier-oscilloscope combination (Hamamatsu R928 P, Tektronix TDS3012C). Kinetics of bleach recovery conditions: Excitation wavelength = 420 nm, analysis wavelength = 450 nm.

### 2.9. Apparent quantum yield calculation

$$\Phi_{\text{AQY}(\text{initial})} = 2 \times \frac{\text{initial oxygen formation rate}}{\text{photon flux}} \times 100\%$$

PF (Photon flux) = A (illuminated area of reaction solution)  $\times$  UPF (unit photon flux)

$$A = 0.5 \times \pi \times r^2 \quad (r = \text{irradiation radius} = 0.02 \text{ m}) = 0.5 \times \pi \times (0.02 \text{ m})^2$$

The  $\text{O}_2$  formation rates of initial 60 s are (measured by Clark electrode)  $0.086 \mu\text{mol s}^{-1}$  for  $\text{Co}_3\text{O}_4$  100,  $0.149 \mu\text{mol s}^{-1}$  for  $\text{Co}_3\text{O}_4$  110 and  $0.132 \mu\text{mol s}^{-1}$  for  $\text{Co}_3\text{O}_4$  112, respectively. UPFs of  $\text{Co}_3\text{O}_4$  100, 110 and 112 are  $1369 \mu\text{mol m}^{-2} \text{ s}^{-1}$ ,  $1412 \mu\text{mol m}^{-2} \text{ s}^{-1}$  and  $1388 \mu\text{mol m}^{-2} \text{ s}^{-1}$ . So, the PF are  $0.43 \mu\text{mol s}^{-1}$  for  $\text{Co}_3\text{O}_4$  100,  $0.44 \mu\text{mol s}^{-1}$  for  $\text{Co}_3\text{O}_4$  110 and  $0.44 \mu\text{mol s}^{-1}$  for  $\text{Co}_3\text{O}_4$  112, respectively. The apparent quantum yields ( $\Phi_{\text{AQY}(\text{initial})}$ ) were calculated to be 20.0% for  $\text{Co}_3\text{O}_4$  100, 33.6% for  $\text{Co}_3\text{O}_4$  110 and 30.35% for  $\text{Co}_3\text{O}_4$  112. After normalized the apparent quantum yield with BET surface area as the equation:  $\text{AQE}_{\text{BET}} = \text{Apparent quantum yield} / \text{BET value of sample} * 100$ . The  $\text{AQE}_{\text{BET}}$  for  $\text{Co}_3\text{O}_4$  100, 110 and 112 are 23.0%, 31.1% and 34.4%, respectively.

In addition, the average photocatalytic  $\text{O}_2$  evolution amount ratios of all three pH conditions for catalysts are one third of the sum of their

photocatalytic  $\text{O}_2$  evolution amount ratio in single pH (5.8 or 7.0 or 9.0). The photocatalytic  $\text{O}_2$  evolution amount are obtained from the GC measurements (Fig. 2b).

### 2.10. Fitting methods for laser photolysis experiments

Transient decay measurements at a single wavelength were used to extract the lifetime components of relevant samples, which were detected by PMT detectors. Each probe wavelength can be fitted by a sum of up to four exponentials with a least-squares-fitting program. The exponential growth or decay process can be expressed in mathematical terms as the following equation.

$$I(t) = c_0 + c_1 e^{\frac{-t}{\tau_1}} + c_2 e^{\frac{-t}{\tau_2}} + c_3 e^{\frac{-t}{\tau_3}} + c_4 e^{\frac{-t}{\tau_4}}$$

where  $I(t)$  is the decay model reflecting the response of the sample to an infinitely short excitation,  $c_0$  is the background,  $c_1, c_2, c_3, c_4$  are the pre-exponential factors reflecting the weight of corresponding characteristic lifetime components of  $\tau_1, \tau_2, \tau_3$  and  $\tau_4$ , respectively [27].

### 2.11. Electrocatalytic water oxidation

The electrochemistry experiments were recorded on a CHI660D electrochemical analyzer connected with a standard three-electrode system where a glassy carbon is the working electrode (GCE, 3 mm in diameter) with  $\text{Ag}/\text{AgCl}$  (saturate KCl,  $E_{\text{RHE}} = E_{\text{Ag}/\text{AgCl}} + 0.197 + \text{pH}^*0.059$ ) and carbon rod electrodes as reference and counter electrodes, respectively. The working electrode was pasted with 0.01 mg catalyst. The process was executed as follow. Disperse 2 mg catalyst powder in the mixture of 780  $\mu\text{L}$  ethanol and 20  $\mu\text{L}$  0.5 wt % nafion, then 4  $\mu\text{L}$  of solution was dropped onto the glassy carbon electrode slowly. CV plots were acquired in 1 M potassium hydroxide (pH 13.6) with different scanning rates. LSV plots were acquired in 1 M potassium hydroxide (pH 13.6) solution from 0 to 0.8 V vs.  $\text{Ag}/\text{AgCl}$  with a scanning rate of  $5 \text{ mV s}^{-1}$ . Electrochemical impedance spectroscopy (EIS) was performed at 0.65 V vs.  $\text{Ag}/\text{AgCl}$  by applying an AC voltage of 5 mV amplitude and frequency range from 100,000 to 0.1 Hz in 1 M potassium hydroxide solution. Tafel slopes were obtained from the LSVs plots through mapping the overpotential  $\eta$  vs  $\log(J)$ .

## 3. Result and discussion

### 3.1. Synthesis and characterization

Spinel  $\text{Co}_3\text{O}_4$  nanocrystals with morphologies of cube, rod and sheet were synthesized according to bottom-up nanotechnologies [14,23,24]. Fig. 1 shows typical scanning electron microscope (SEM), transmission electron microscopy (TEM), high resolution transmission electron microscopy (HRTEM) and fast Fourier transformation (FFT) images of  $\text{Co}_3\text{O}_4$  nanocubes, nanorods and nanosheets. As shown in Fig. 1a and d,  $\text{Co}_3\text{O}_4$  nanocubes are well-dispersed with a well-proportioned size of ca. 30–40 nm and are exposed six {100} facets, which are the sole facets normal to two sets of crossing (220) facets.

The average diameter and length of  $\text{Co}_3\text{O}_4$  nanorods are around 10–15 nm and 100 nm, respectively (Fig. 1b), whereas Fig. 1c demonstrate that the as-prepared  $\text{Co}_3\text{O}_4$  nanosheets possess an average edge length and thickness of ca. 200–250 nm and 10–15 nm with hexagons, respectively. The primarily exposed crystal planes of as-synthesized  $\text{Co}_3\text{O}_4$  nanorods are {110}, which are normal to the set of (222) planes and the relevant set of (311) planes (Fig. 1e). For  $\text{Co}_3\text{O}_4$  nanosheets, Fig. 1f shows that the dominant exposed planes are {112}, which are the only facets normal to the two orthogonal sets of (220) and (222) facets.  $\text{Co}_3\text{O}_4$  nanocubes, nanorods and nanosheets are hereinafter named  $\text{Co}_3\text{O}_4$  100, 110 and 112, respectively, according to their dominant exposed crystal planes (Fig. 1g-i).

In Fig. S1a, the powder X-ray diffraction (PXRD) patterns of  $\text{Co}_3\text{O}_4$

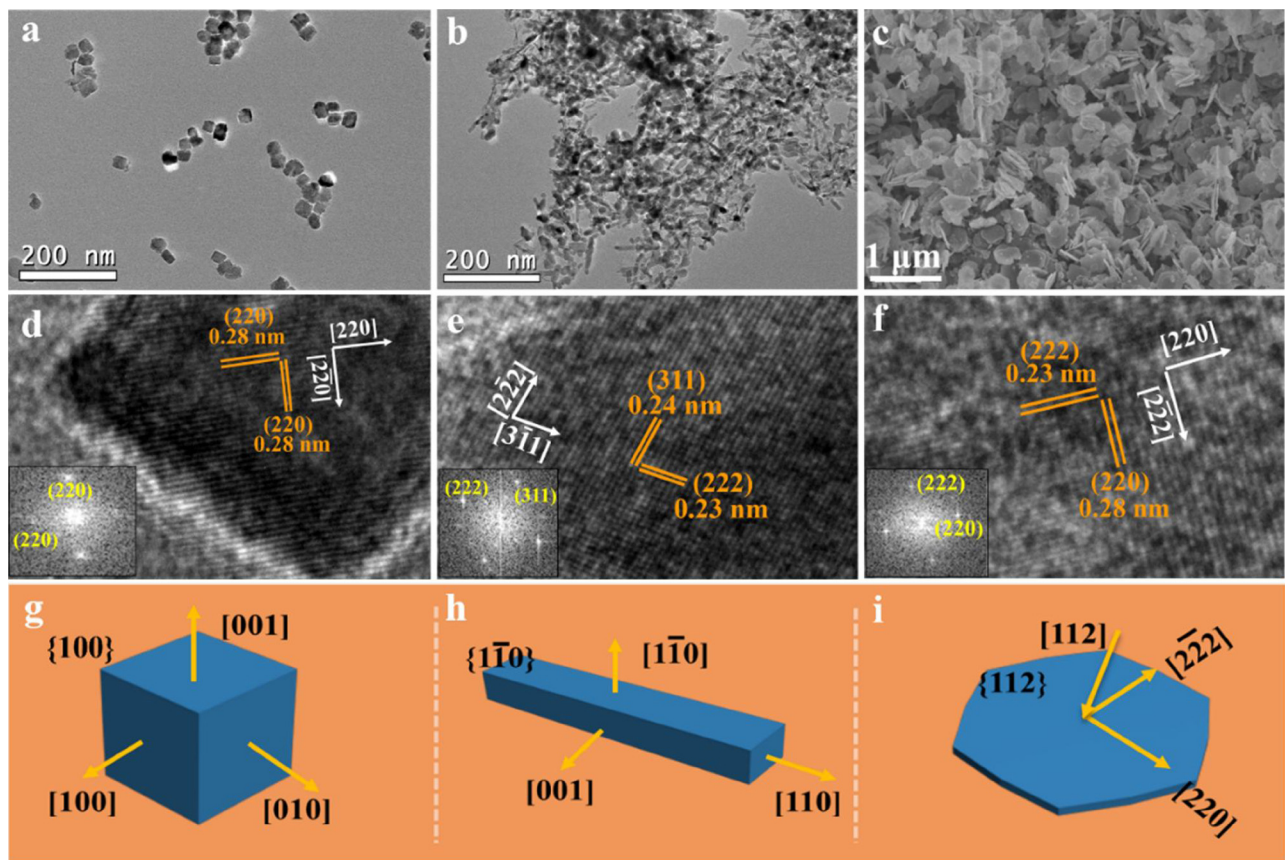


**Fig. 1.** TEM images of (a)  $\text{Co}_3\text{O}_4$  100 and (b) 110. SEM images of (c)  $\text{Co}_3\text{O}_4$  112. HRTEM images of (d)  $\text{Co}_3\text{O}_4$  100, (e)  $\text{Co}_3\text{O}_4$  110 and (f)  $\text{Co}_3\text{O}_4$  112. The insets in (d), (e) and (f) are the relevant FFT images. Schematic representation of (g)  $\text{Co}_3\text{O}_4$  100, (h) 110 and (i) 112. [uvw] is an index of a specified crystal axis and (hkl) is an index of a specified crystal plane, while {hkl} indicates a set of group crystal planes with the same atomic configuration.

100, 110, and 112 are identified well with the values of standard diffraction peaks of  $\text{Co}_3\text{O}_4$  in the literature (JCPDS# 76-1802, lattice constant  $a = 8.072 \text{ \AA}$ ), indicating the pure spinel structure with face-centered cubic (fcc) phase in a space group of  $Fd\bar{3}m$  of three  $\text{Co}_3\text{O}_4$  samples [12]. X-ray photoelectron spectroscopy (XPS) analysis reveals the detailed states of elements in the surface of the  $\text{Co}_3\text{O}_4$  samples. As shown in Fig. S1b, the Co 2p bonding states of  $\text{Co}_3\text{O}_4$  100, 110, and 112 are almost same. Two dominant peaks are located at 780.1 eV for Co  $2p_{3/2}$  and 795.2 eV for Co  $2p_{1/2}$  with a separation of  $2p_{1/2}-2p_{3/2}$  spin-orbital splitting of 15.1 eV, demonstrating the coexistence of  $\text{Co}^{3+}$  and  $\text{Co}^{2+}$  species [28]. The absence of the prominent shakeup satellite peaks in Co 2p does manifest the formation of  $\text{Co}_3\text{O}_4$  phase [28]. The Brunauer-Emmett-Teller (BET) surface areas of  $\text{Co}_3\text{O}_4$  100, 112 and 110 are  $87.0 \text{ m}^2 \text{ g}^{-1}$ ,  $88.2 \text{ m}^2 \text{ g}^{-1}$  and  $107.8 \text{ m}^2 \text{ g}^{-1}$ , respectively (Table S1).

### 3.2. Photocatalytic water oxidation

Visible-light driven photocatalytic water oxidation (PWO) of  $\text{Co}_3\text{O}_4$  was performed under the  $[\text{Ru}(\text{bpy})_3]^{2+}-\text{S}_2\text{O}_8^{2-}$  system, in which  $[\text{Ru}(\text{bpy})_3]^{2+}$  plays a role as photosensitizer and  $\text{Na}_2\text{S}_2\text{O}_8$  serves as a two-electron oxidant [29–31]. In a typical photocatalytic water oxidation cycle (Scheme 1), photoexcited orange  $[\text{Ru}(\text{bpy})_3]^{2+}$  (i.e.,  $[\text{Ru}(\text{bpy})_3]^{2+,*}$ ) is oxidized by  $\text{Na}_2\text{S}_2\text{O}_8$  to produce green photoinduced oxidant  $[\text{Ru}(\text{bpy})_3]^{3+}$ ,  $\text{SO}_4^{2-}$ , and  $\text{SO}_4^{2-}$ . Then the generated in-situ sulfate radical ( $\text{SO}_4^{2-}\cdot$ ) further reacts with  $[\text{Ru}(\text{bpy})_3]^{2+}$  to form additional  $[\text{Ru}(\text{bpy})_3]^{3+}$ . The produced  $[\text{Ru}(\text{bpy})_3]^{3+}$  oxidize WOCs to high valence state, then following the formation of oxygen. The restored  $[\text{Ru}(\text{bpy})_3]^{2+}$  starts next cycle again.

Oxygen evolution of  $\text{Co}_3\text{O}_4$  catalysts was monitored online in

solution with a calibrated Clark electrode. As shown in Fig. 2a, different oxygen evolution curves were detected on  $\text{Co}_3\text{O}_4$  nanocrystals with different shapes in a borate buffer solution (pH 9.0). A maximum TOF (initial 60 s turnover frequency, normalized by surface area) of  $0.50 \mu\text{mol m}_{\text{cat}}^{-2} \text{ s}^{-1}$  is observed towards  $\text{Co}_3\text{O}_4$  112 and a similar TOF of  $0.46 \mu\text{mol m}_{\text{cat}}^{-2} \text{ s}^{-1}$  is obtained over  $\text{Co}_3\text{O}_4$  110, while  $\text{Co}_3\text{O}_4$  100 shows a minimum TOF of  $0.33 \mu\text{mol m}_{\text{cat}}^{-2} \text{ s}^{-1}$ . The apparent quantum yield normalized with BET surface area ( $\text{AQE}_{\text{BET}}$ ) of  $\text{Co}_3\text{O}_4$  112, 110 and 100 are 34.4%, 31.1% and 23.0%, respectively. The control experiment without addition of  $\text{Co}_3\text{O}_4$  was performed, and only a few amounts of  $\text{O}_2$  evolution were detected. Photocatalytic oxygen evolution was also tested under moderate acidic (pH 5.8), neutral (pH 7.0) and alkaline conditions (pH 9.0) and the output of oxygen was measured by gas chromatography. The same sequence is obtained for all catalytic activity tests, in which  $\text{Co}_3\text{O}_4$  110 possesses a good activity close to  $\text{Co}_3\text{O}_4$  112, and  $\text{Co}_3\text{O}_4$  100 displays a relatively poor activity (Fig. 2b, Table S2). The average photocatalytic  $\text{O}_2$  evolution amount ratio of all three pH conditions for  $\text{Co}_3\text{O}_4$  112 to  $\text{Co}_3\text{O}_4$  110 is ca. 1.1, whereas this value is ca. 1.8 for  $\text{Co}_3\text{O}_4$  112 to  $\text{Co}_3\text{O}_4$  100. It demonstrates that the different crystal planes exert significant influence on the catalytic activity of  $\text{Co}_3\text{O}_4$  nanocrystals.

Fig. S2 displays the adsorption interactions between the  $\text{Co}_3\text{O}_4$  catalysts and photosensitizer. Minimum absorbance of  $[\text{Ru}(\text{bpy})_3]\text{Cl}_2$  after being treated with  $\text{Co}_3\text{O}_4$  100 indicates the strongest adsorption between photosensitizer and the surface of  $\text{Co}_3\text{O}_4$  100, whereas the weakest adsorption between the surface of  $\text{Co}_3\text{O}_4$  112 and photosensitizer is shown by the maximum absorbance among the three samples. The sequence of adsorption intensities of photosensitizer on different  $\text{Co}_3\text{O}_4$  samples is not in accordance with the catalytic activity order, indicating that the catalysts' photocatalytic activities are not

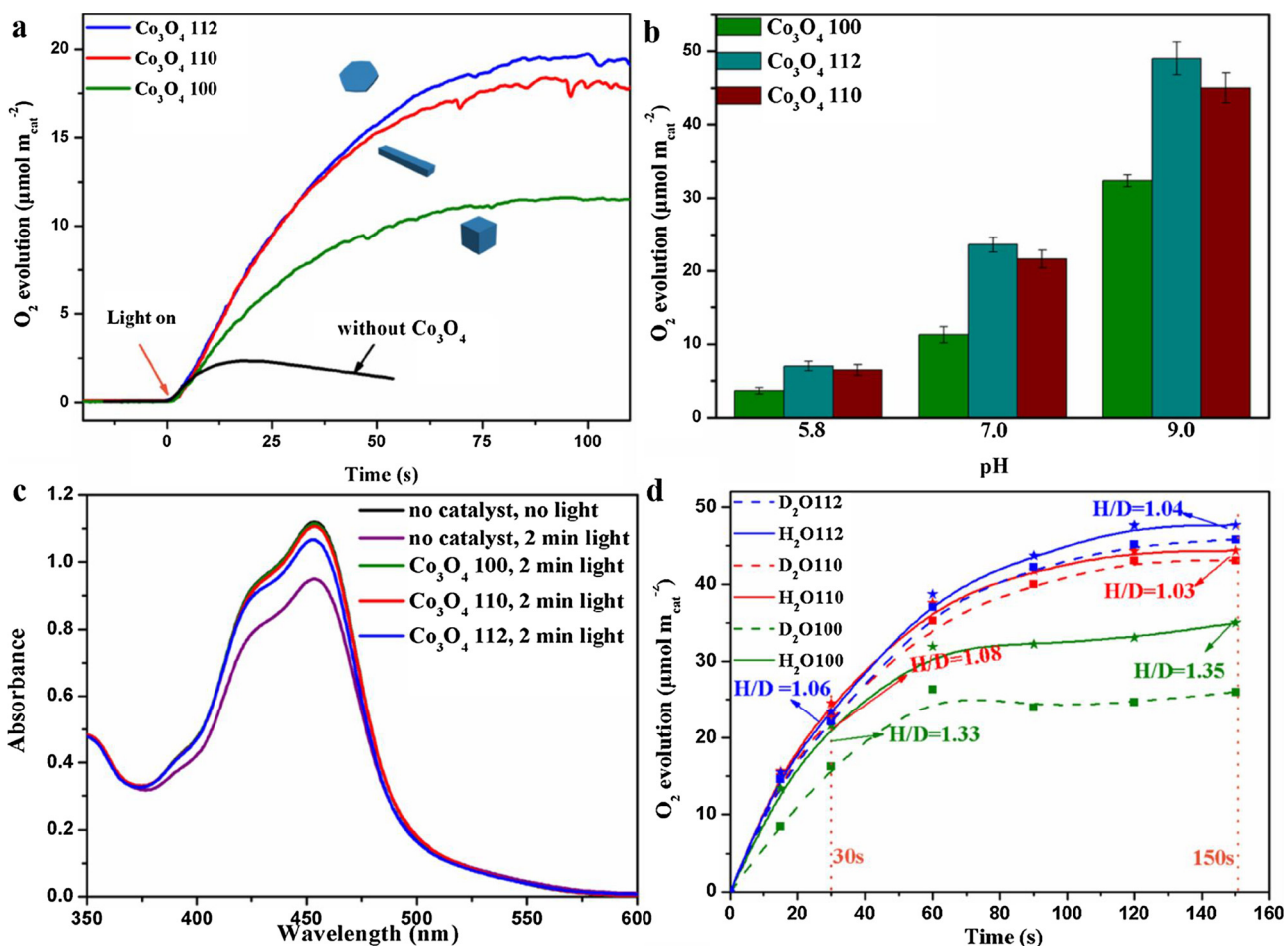
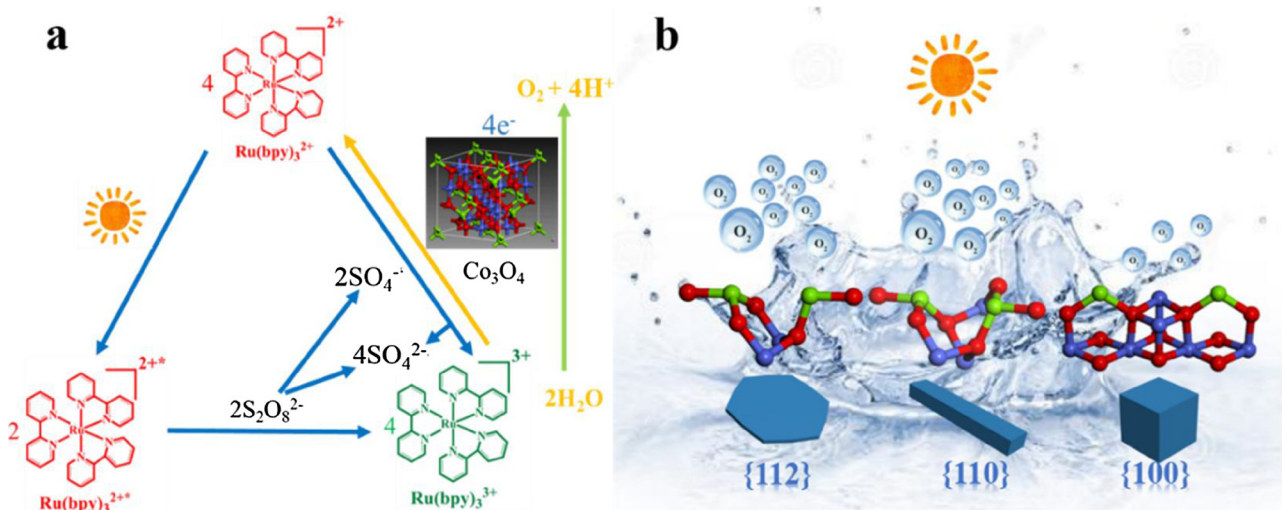


**Fig. 2.** (a) Time courses of  $\text{O}_2$  evolution measured by the Clark electrode system in borate buffer (pH 9.0), the oxygen evolution amount of blank (without  $\text{Co}_3\text{O}_4$ ) was normalized by the BET surface area of  $\text{Co}_3\text{O}_4$  100; (b) photocatalytic oxygen evolution amount of  $\text{Co}_3\text{O}_4$  catalysts in different buffer solutions ( $\text{NaHCO}_3$ - $\text{Na}_2\text{SiF}_6$ , pH 5.8; phosphate, pH 7.0; borate buffer, pH 9.0) measured by gas chromatography; (c) UV-vis spectra of  $[\text{Ru}(\text{bpy})_3]\text{Cl}_2$ ,  $[\text{Ru}(\text{bpy})_3]\text{Cl}_2 + \text{Na}_2\text{S}_2\text{O}_8$  after illumination and  $[\text{Ru}(\text{bpy})_3]\text{Cl}_2 + \text{Na}_2\text{S}_2\text{O}_8$  with  $\text{Co}_3\text{O}_4$  112, 110 and 100 after illumination. (d) Photocatalytic time courses of  $\text{O}_2$  evolution in the borate buffer of aqueous solution (pH 9.0) and deuterium aqueous solution (pD 9.0) containing  $\text{Na}_2\text{S}_2\text{O}_8$  (5.0 mM),  $[\text{Ru}(\text{bpy})_3]\text{Cl}_2$  (1.0 mM) and (3 mg) catalysts.



**Scheme 1.** (a) Photocatalytic water oxidation cycle in the  $[\text{Ru}(\text{bpy})_3]^{2+}/\text{S}_2\text{O}_8^{2-}$  protocol system with catalyst  $\text{Co}_3\text{O}_4$ ; (b) Oxygen evolution from three  $\text{Co}_3\text{O}_4$  samples.

particularly related to the interactions between the catalysts and the photosensitizer. Once  $[\text{Ru}(\text{bpy})_3]^{3+}$  is formed, electrons transfer from WOCs to  $[\text{Ru}(\text{bpy})_3]^{3+}$  to form WOCs in high valence state. Then, the water is oxidized by WOCs for oxygen evolution. However, the photo-induced oxidant  $[\text{Ru}(\text{bpy})_3]^{3+}$  can be degraded by nucleophilic attack of  $\text{OH}^-$  or water, which competes with the course that WOCs are oxidized by  $[\text{Ru}(\text{bpy})_3]^{3+}$ . Thus, we can determine the rate-determining step (RDS) by comparing the decomposition extent of photosensitizer after photocatalytic water oxidation. If the oxygen evolution sequence of  $\text{Co}_3\text{O}_4$  112, 110 and 100 are different from the order of the remaining amount of photosensitizer after reaction, the RDS of photocatalytic water oxidation will be the step that the water is oxidized by high-valence catalysts to form  $\text{O}_2$ . UV-vis spectra of remaining  $[\text{Ru}(\text{bpy})_3]^{2+}$  in different mixtures are shown in Fig. 2c, the sequence of the remaining amount of  $[\text{Ru}(\text{bpy})_3]^{2+}$  of different  $\text{Co}_3\text{O}_4$  mixtures is different with the order of oxygen evolution activities of these  $\text{Co}_3\text{O}_4$  mixtures. Therefore, the RDS of water oxidation in the present system is the step of  $\text{O}_2$  generation rather than the step that catalyst is oxidized to high-valence state, which is consistent with the consensus in previous publications [29]. Meanwhile, the removal of four protons (break of four O–H bonds) from water is required in water oxidation. The more difficult this process is, the more pronounced deuterium kinetic isotope effect is when  $\text{H}_2\text{O}$  is replaced by  $\text{D}_2\text{O}$  for oxygen evolution. As shown in Fig. 2d,  $\text{Co}_3\text{O}_4$  100 shows a deuterium kinetic isotope effect ( $\text{KIE} = k_{\text{H}_2\text{O}}/k_{\text{D}_2\text{O}} = 0.77 \text{ s}^{-1}/0.58 \text{ s}^{-1}$ , initial 30 s) of 1.33 while this KIE value for  $\text{Co}_3\text{O}_4$  110 and 112 are 1.08 and 1.06, respectively, revealing that breakage of the O–H bond is relatively harder for  $\text{Co}_3\text{O}_4$  100 than those of  $\text{Co}_3\text{O}_4$  110 and 112.[32,33]

Real-time laser flash photolysis experiments were further employed to investigate the fast photocatalytic-electron transfer during the PWO, and the dynamically photocatalytic courses of three  $\text{Co}_3\text{O}_4$  are distinguished in nanosecond scale. When flash is triggered,  $[\text{Ru}(\text{bpy})_3]^{2+}$  transfers into photoexcited  $[\text{Ru}(\text{bpy})_3]^{2+*}$ , then return to the ground state by fluorescence quenching spontaneously. As is shown in Figs. 3a, S3 and S4, the lifetime of fluorescence recovery is 378.6 ns for  $[\text{Ru}(\text{bpy})_3]\text{Cl}_2$ . However, the generated  $[\text{Ru}(\text{bpy})_3]^{2+*}$  can be oxidized to  $[\text{Ru}(\text{bpy})_3]^{3+}$  by  $\text{S}_2\text{O}_8^{2-}$  and the  $\Delta\text{O.D.}$  values keep constant, as shown in Fig. 3b.  $[\text{Ru}(\text{bpy})_3]^{3+}$  cannot recover to  $[\text{Ru}(\text{bpy})_3]^{2+}$  in the absence of catalyst. When  $\text{Co}_3\text{O}_4$  catalysts are added, the bleaching recovery of photosensitizer is observed, revealing that the  $[\text{Ru}(\text{bpy})_3]^{3+}$  turns into  $[\text{Ru}(\text{bpy})_3]^{2+}$  through receiving the electrons from  $\text{Co}_3\text{O}_4$  catalysts (Fig. 3c and d) [34]. As shown in Fig. 3d, the fastest bleaching recovery is obtained by the mixture of  $[\text{Ru}(\text{bpy})_3]^{2+} + \text{S}_2\text{O}_8^{2-} + \text{Co}_3\text{O}_4$  112 and the recovery rate of  $[\text{Ru}(\text{bpy})_3]^{2+} + \text{S}_2\text{O}_8^{2-} + \text{Co}_3\text{O}_4$  110 is close to that of 112, suggesting relatively faster electron transfer from water to high-valence  $\text{Co}_3\text{O}_4$  112 and 110. The slowest bleaching recovery is shown by the mixture of  $[\text{Ru}(\text{bpy})_3]^{2+} + \text{S}_2\text{O}_8^{2-} + \text{Co}_3\text{O}_4$  100, revealing that oxidized  $\text{Co}_3\text{O}_4$  100 has the slowest electron extraction from water among three  $\text{Co}_3\text{O}_4$  samples. The lifetime of bleaching recovery is 299.1 ns for  $\text{Co}_3\text{O}_4$  112 and 352.1 ns for  $\text{Co}_3\text{O}_4$  110 (Fig. S5), however, this value cannot be obtained from the mixture containing  $\text{Co}_3\text{O}_4$  100 due to the incomplete recovery, suggesting that the activity of  $\text{Co}_3\text{O}_4$  100 is poorer than those of  $\text{Co}_3\text{O}_4$  112 and 110. Overall,  $\text{Co}_3\text{O}_4$  100 demonstrates a clear electron transfer gap.

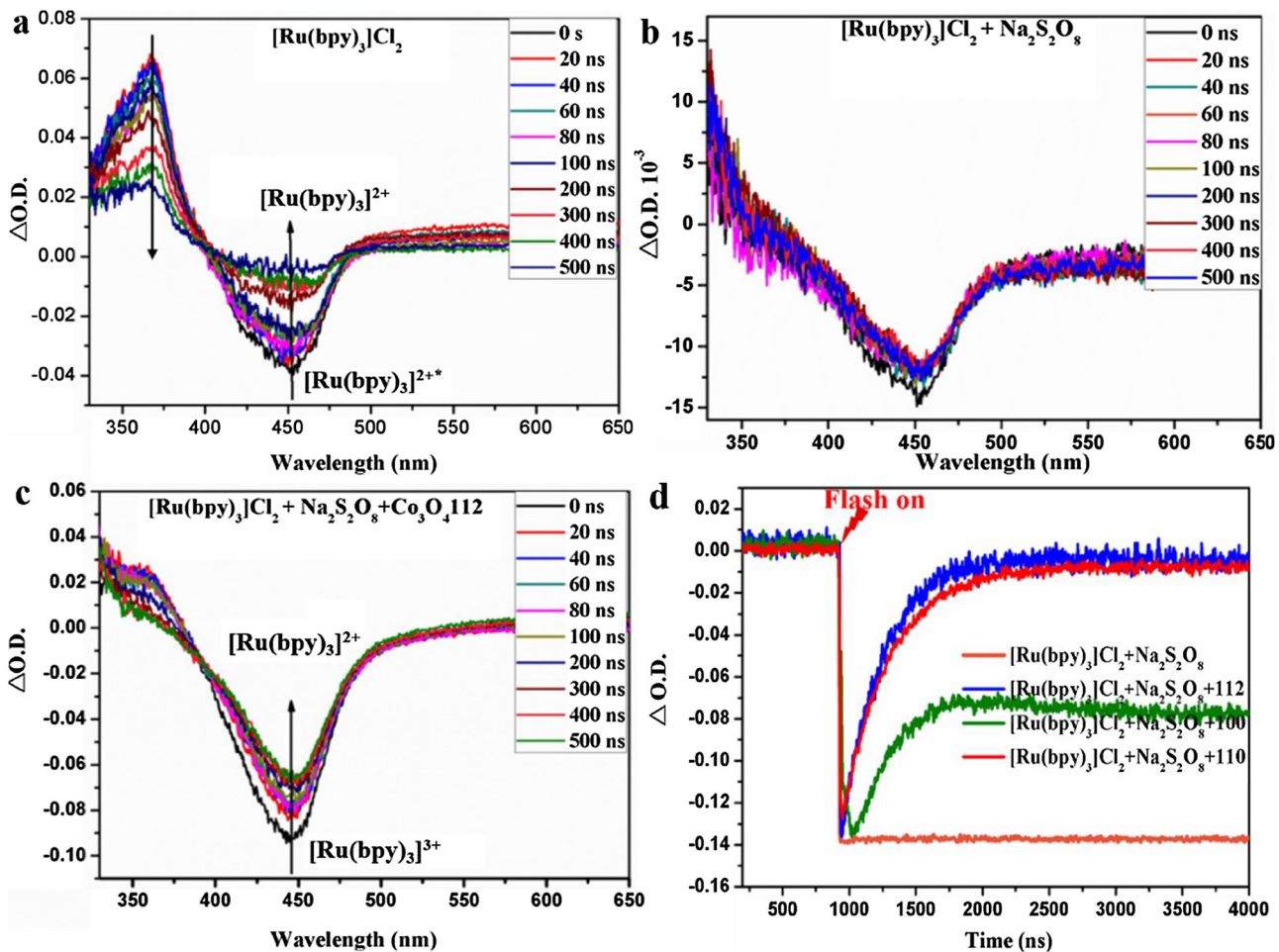


**Fig. 3.** (a) Transient absorption spectra of  $[\text{Ru}(\text{bpy})_3]\text{Cl}_2$ , (b)  $[\text{Ru}(\text{bpy})_3]\text{Cl}_2 + \text{Na}_2\text{S}_2\text{O}_8$  mixture, (c)  $[\text{Ru}(\text{bpy})_3]\text{Cl}_2 + \text{Na}_2\text{S}_2\text{O}_8 + \text{Co}_3\text{O}_4$  112 mixture, and (d) the nanosecond recovery kinetics of transient bleaching recovery for photosensitizer monitored at 450 nm, the excitation wavelength is 420 nm.

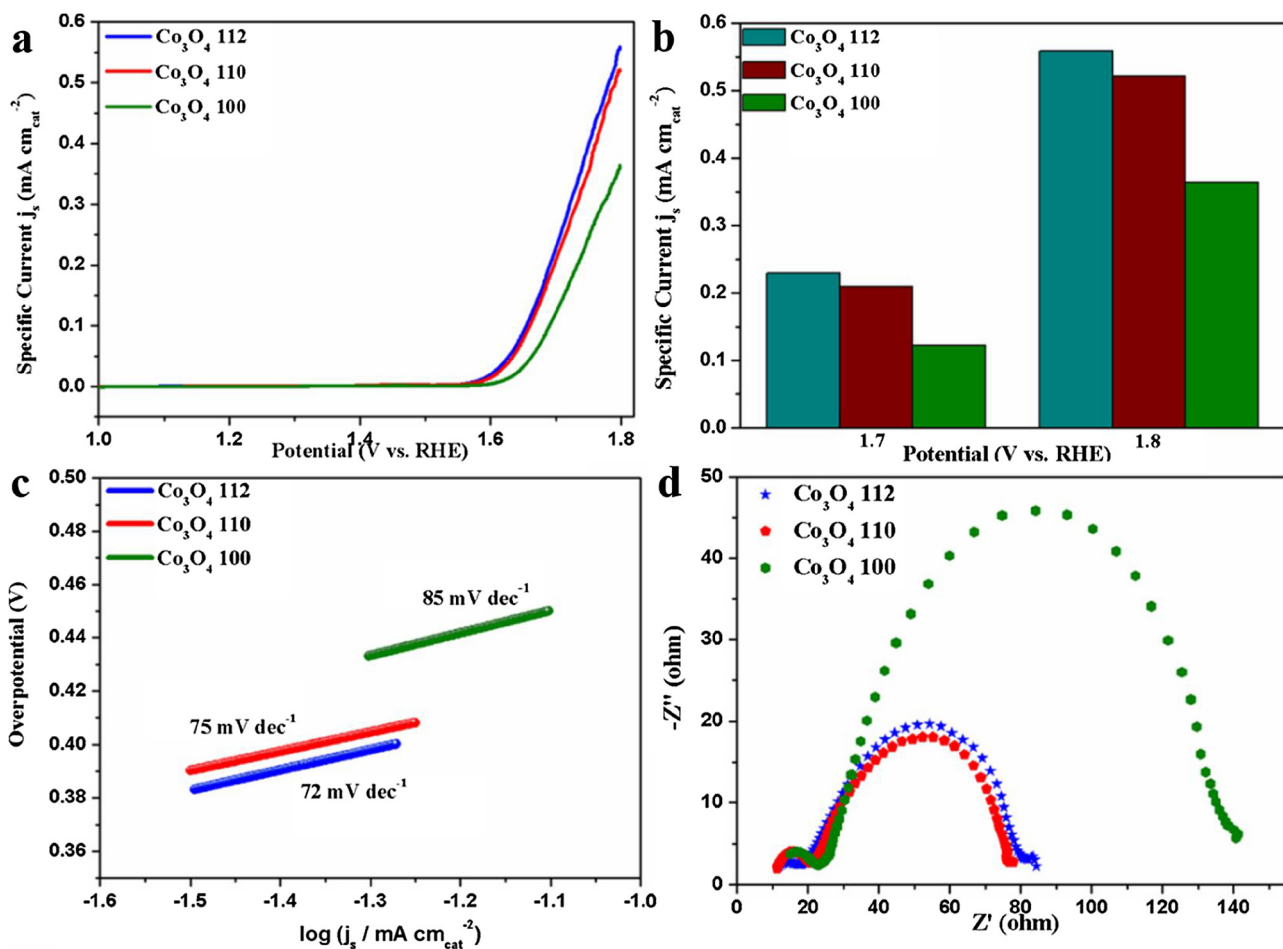


**Fig. 4.** (a) Linear sweep voltammograms (LSV) of three  $\text{Co}_3\text{O}_4$  samples, (b) specific current density of three  $\text{Co}_3\text{O}_4$  at different potentials, (c) Tafel slopes of three  $\text{Co}_3\text{O}_4$ , (d) Nyquist diagrams of EIS for three  $\text{Co}_3\text{O}_4$ .

### 3.3. Electrocatalytic water oxidation

The electrochemistry experiments were recorded using a three-electrode system where a glassy carbon is the working electrode, Ag/AgCl electrode as reference and carbon rod as counter electrodes, respectively. A distinct phenomenon is that the photocatalytic activities of  $\text{Co}_3\text{O}_4$  110 and 112 are similar, while the photocatalytic performance of  $\text{Co}_3\text{O}_4$  100 is obviously poorer than those of  $\text{Co}_3\text{O}_4$  110 and 112. To clarify the universality of this rule, a series of electrochemical water oxidation (EWO) experiments were carried out as follow. Fig. S6 demonstrates that the water oxidation processes catalyzed by three  $\text{Co}_3\text{O}_4$  samples are all surface controlled reactions and that the oxidation peaks are surface reaction limited response [35]. As shown in Fig. 4,  $\text{Co}_3\text{O}_4$  112 and 110 always show comparative EWO activity, and their catalytic performances are obviously better than that of  $\text{Co}_3\text{O}_4$  100. In Fig. 4a, linear sweep voltammogram curves of three  $\text{Co}_3\text{O}_4$  samples show that the electrocatalytic water oxidation activity of  $\text{Co}_3\text{O}_4$  112 and 110 are similar, and the activity of  $\text{Co}_3\text{O}_4$  100 is clearly inferior to those of  $\text{Co}_3\text{O}_4$  112 and 110. The specific current densities at the potential of 1.7 V of  $\text{Co}_3\text{O}_4$  112 and 110 are 0.23 and 0.21 mA cm $_{cat}^{-2}$ , respectively, while  $\text{Co}_3\text{O}_4$  100 is only 0.12 mA cm $_{cat}^{-2}$ . The specific current densities of  $\text{Co}_3\text{O}_4$  112, 110 and 100 at the potential of 1.8 V are 0.56, 0.52 and 0.36 mA cm $_{cat}^{-2}$ , respectively (Fig. 4b). The Tafel slopes are 72 mV dec $^{-1}$  for  $\text{Co}_3\text{O}_4$  112 and 75 mV dec $^{-1}$  for  $\text{Co}_3\text{O}_4$  110, whereas 85 mV dec $^{-1}$  for  $\text{Co}_3\text{O}_4$  100 (Fig. 4c). The curvature radius of electrochemical impedance spectroscopy (EIS) is significantly related to the charge transfer resistance in the water oxidation process, that is, the smaller curvature radius represents faster charge transport speed. As

the Nyquist diagrams shown in Figs. 4d and S7, catalyst  $\text{Co}_3\text{O}_4$  100 has a larger charge transfer resistance than those of  $\text{Co}_3\text{O}_4$  112 and 110, suggesting  $\text{Co}_3\text{O}_4$  112 and 110 have better water oxidation activity [36]. In all, the electrocatalytic activity order of three  $\text{Co}_3\text{O}_4$  samples is consistent with their photocatalytic water oxidation activity order. The general activity sequence rule illustrates that the catalytic performances of samples  $\text{Co}_3\text{O}_4$  112, 110 and 100 are not associated with reaction systems but closely with the surface states of three  $\text{Co}_3\text{O}_4$  catalysts.

### 3.4. Surface state analysis of $\text{Co}_3\text{O}_4$ catalysts

To unravel the above activity order discipline, a series of characterization methods were carried out concerning of surface properties of three  $\text{Co}_3\text{O}_4$  samples. We evidenced the difference in water-surface interaction modes of three  $\text{Co}_3\text{O}_4$  samples via macroscopic water adsorption on the  $\text{Co}_3\text{O}_4$  100, 110 and 112 surfaces monitored by water contact angle measurements (Fig. S8).

Results reveal that  $\text{Co}_3\text{O}_4$  112 ( $17.0^\circ$ ) and  $\text{Co}_3\text{O}_4$  110 ( $18.4^\circ$ ) have similar hydrophilic property, which is superior to that of  $\text{Co}_3\text{O}_4$  100 ( $48.8^\circ$ ). Fig. 5a exhibits the X-ray photoelectron spectra of O1 s of three  $\text{Co}_3\text{O}_4$  samples. Each O 1 s spectrum of  $\text{Co}_3\text{O}_4$  100, 110, and 112 is deconvoluted into three dominant peaks. The peaks at ca. 530.2, 531.5 and 532.4 eV are assigned to lattice oxygen species, hydroxide species ( $-OH$ ) and adsorbed water at the surface of  $\text{Co}_3\text{O}_4$  (Fig. 5a) [28]. The area ratios of  $-OH$  to adsorbed water in different  $\text{Co}_3\text{O}_4$  samples are different, which means that three  $\text{Co}_3\text{O}_4$  samples have intrinsically different surface states, especially for absorbing and activating of water [37]. In Fig. 5b, similar ratios of  $-OH$  zone to adsorbed water are found

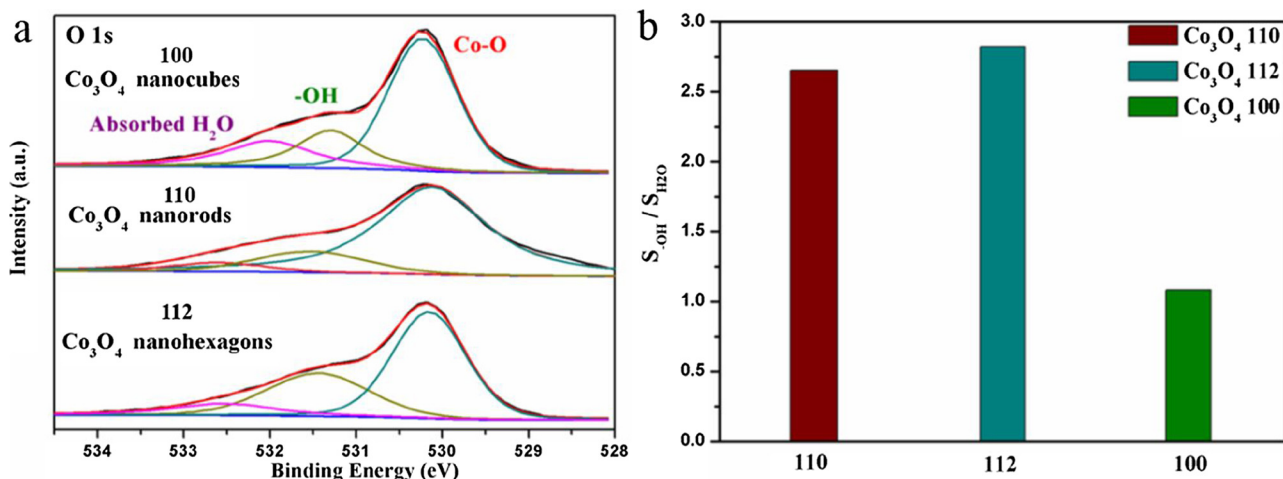


Fig. 5. (a) XPS O 1s spectra of  $\text{Co}_3\text{O}_4$  100, 110 and 112; (d) The ratio of the area of hydroxyl group and absorbed water in O1 s spectra of  $\text{Co}_3\text{O}_4$  100, 110 and 112.

both in  $\text{Co}_3\text{O}_4$  110 and 112 with values of 2.7 and 2.8, respectively, while the value of  $\text{Co}_3\text{O}_4$  100 is 1.3. The result suggests that the ability to adsorb, activate and dissociate water to  $-\text{OH}$  is stronger on the surface of  $\text{Co}_3\text{O}_4$  110 and 112 than that in  $\text{Co}_3\text{O}_4$  100 [37].

The surface properties of three samples were further characterized by  $\zeta$  potential measurements in the borate buffer (pH 9.0). The  $\zeta$  potential values of  $\text{Co}_3\text{O}_4$  100, 110 and 112 are  $-37.3\text{ mV}$ ,  $-30.7\text{ mV}$  and  $-31.9\text{ mV}$ , respectively (Fig. S9). Similar  $\zeta$  potential values of  $\text{Co}_3\text{O}_4$  110 and 112 indicate that they form a similar electric double layer in the buffer solution with similar surface properties [38].  $\text{Co}_3\text{O}_4$  100 with a more negative  $\zeta$  potential value is ascribed to relatively different surface property. The above experimental results demonstrate {110} and {112} crystal planes of  $\text{Co}_3\text{O}_4$  possess the similar surface nature, while {100} planes of  $\text{Co}_3\text{O}_4$  does not have.

### 3.5. Identification of the main active site of $\text{Co}_3\text{O}_4$ in photocatalytic water oxidation

To gain in-depth understanding of the activity rule of  $\text{Co}_3\text{O}_4$  catalysts, we investigated whether the  $\text{Co}^{2+}$  in the tetrahedral site ( $\text{Co}_{\text{td}}^{2+}$ ) or  $\text{Co}^{3+}$  in the octahedral site ( $\text{Co}_{\text{oh}}^{3+}$ ) of spinel structure acts as the main active site in the photocatalytic water oxidation (Figs. 6 and S10). We synthesized spinel  $\text{ZnCo}_2\text{O}_4$  and  $\text{CoAl}_2\text{O}_4$  by replacing the  $\text{Co}_{\text{td}}^{2+}$  and  $\text{Co}_{\text{oh}}^{3+}$  of  $\text{Co}_3\text{O}_4$  with inactive  $\text{Zn}^{2+}$  and  $\text{Al}^{3+}$ , respectively [26]. Fig. 6a shows that  $\text{ZnCo}_2\text{O}_4$  and  $\text{CoAl}_2\text{O}_4$  have similar PXRD patterns, and they are identical well with that of  $\text{Co}_3\text{O}_4$  112, suggesting a typical cubic-spinel structure of  $\text{ZnCo}_2\text{O}_4$  and  $\text{CoAl}_2\text{O}_4$  [39,40]. As shown in Fig. 6b, the two peaks of 797.4 eV of  $\text{Co} 2p_{1/2}$  and 781.3 eV of  $\text{Co} 2p_{3/2}$  in  $\text{CoAl}_2\text{O}_4$  reveal that the  $\text{Co}^{2+}$  is preserved in  $\text{CoAl}_2\text{O}_4$  as we expected. The  $\text{Co} 2p_{1/2}$  peak and the  $\text{Co} 2p_{3/2}$  peak of  $\text{ZnCo}_2\text{O}_4$  are 795.1 eV and 780.1 eV, respectively, demonstrating the primary existence of  $\text{Co}^{3+}$  in

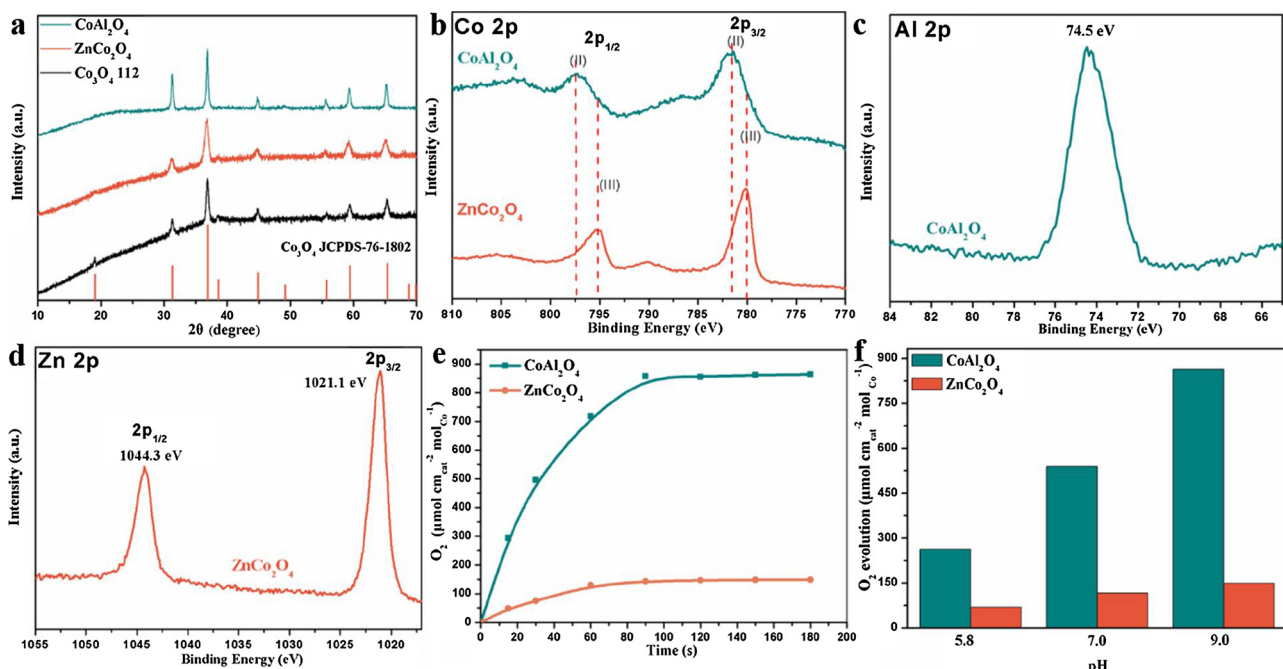


Fig. 6. (a) PXRD patterns of  $\text{CoAl}_2\text{O}_4$ ,  $\text{ZnCo}_2\text{O}_4$  and  $\text{Co}_3\text{O}_4$  112; (b) XPS Co 2p spectra of  $\text{CoAl}_2\text{O}_4$  and  $\text{ZnCo}_2\text{O}_4$ ; (c) XPS Al 2p spectrum of  $\text{CoAl}_2\text{O}_4$ ; (d) XPS Zn 2p spectrum of  $\text{ZnCo}_2\text{O}_4$ ; (e) Time courses of  $\text{O}_2$  evolution under photoirradiation in a borate buffer solution (pH 9.0, 10.0 mL) containing  $\text{Na}_2\text{S}_2\text{O}_8$  (5.0 mM),  $[\text{Ru}(\text{bpy})_3]\text{Cl}_2$  (1.0 mM) and  $\text{CoAl}_2\text{O}_4$  / $\text{ZnCo}_2\text{O}_4$  (0.3 g  $\text{L}^{-1}$ ); (f) Oxygen evolution amount catalyzed by  $\text{CoAl}_2\text{O}_4/\text{ZnCo}_2\text{O}_4$  catalysts in different buffer solutions ( $\text{NaHCO}_3$ - $\text{Na}_2\text{SiF}_6$ , pH 5.8; phosphate, pH 7.0; borate buffer, pH 9.0) measured by gas chromatography.

$\text{ZnCo}_2\text{O}_4$  [41]. The binding energy of 74.5 eV contributes the dominating presence of octahedral  $\text{Al}^{3+}$  in  $\text{CoAl}_2\text{O}_4$  (Fig. 6c) [42]. The binding energy values of 1021.1 eV and 1044.3 eV represent spin-orbit doublets of  $\text{Zn } 2p_{3/2}$  and  $\text{Zn } 2p_{1/2}$  of tetrahedral  $\text{Zn}^{2+}$  state in  $\text{ZnCo}_2\text{O}_4$ , respectively (Fig. 6d) [43]. As shown in Fig. S10a and b, both  $\text{ZnCo}_2\text{O}_4$  and  $\text{CoAl}_2\text{O}_4$  do not have regular morphologies. It should be noted that the main factor that influence catalytic performance of  $\text{ZnCo}_2\text{O}_4$  and  $\text{CoAl}_2\text{O}_4$  is not their morphologies because they are different substances. The BET surface areas of  $\text{ZnCo}_2\text{O}_4$  and  $\text{CoAl}_2\text{O}_4$  were measured as  $47.6 \text{ m}^2 \text{ g}^{-1}$  and  $31.2 \text{ m}^2 \text{ g}^{-1}$ , respectively (Table S1). The energy dispersive X-ray (EDX) results show that the metal element ratios are  $\text{Zn:Co} = 1:1.9$  for  $\text{ZnCo}_2\text{O}_4$  and  $\text{Co:Al} = 1:2.2$  for  $\text{CoAl}_2\text{O}_4$ , which is in accord with the metal ratios in the synthetic substrate ( $\text{Zn:Co} = 1:2$ ,  $\text{Co:Al} = 1:2$ ), confirming the successfully controlled synthesis of  $\text{ZnCo}_2\text{O}_4$  and  $\text{CoAl}_2\text{O}_4$  (Fig. S10c and d).

The water oxidation activities of  $\text{ZnCo}_2\text{O}_4$  and  $\text{CoAl}_2\text{O}_4$  were evaluated in the  $[\text{Ru}(\text{bpy})_3]^{2+}-\text{S}_2\text{O}_8^{2-}$  system (Table S3). Given that the  $\text{Zn}^{2+}$  and  $\text{Al}^{3+}$  are inactive in catalyzing water oxidation, the  $\text{Co}^{3+}_{\text{Oh}}$  and  $\text{Co}^{2+}_{\text{Td}}$  should be responsible for the water oxidation performance of  $\text{ZnCo}_2\text{O}_4$  and  $\text{CoAl}_2\text{O}_4$ , respectively [26]. Fig. 6e shows that the photocatalytic oxygen evolution amount of  $\text{CoAl}_2\text{O}_4$  is almost 6.5 times higher than that of  $\text{ZnCo}_2\text{O}_4$  in borate buffer (pH 9.0). The oxygen evolution TOF (Initial 60 s turnover frequency, normalized by surface area and the number of Co ions) of  $\text{CoAl}_2\text{O}_4$  and  $\text{ZnCo}_2\text{O}_4$  are 12.0 and  $2.2 \mu\text{mol m}_{\text{cat}}^{-2} \text{ mol}_{\text{Co}}^{-1} \text{ s}^{-1}$ , respectively. Moreover, this water oxidation activity difference between  $\text{CoAl}_2\text{O}_4$  and  $\text{ZnCo}_2\text{O}_4$  is universal in the pH range from 5.8 to 9.0 (Fig. 6f). These results show that the  $\text{Co}^{2+}_{\text{Td}}$  in spinel  $\text{Co}_3\text{O}_4$  is more active than  $\text{Co}^{3+}_{\text{Oh}}$ , and  $\text{Co}^{2+}_{\text{Td}}$  should be the main active site for photocatalytic water oxidation.

### 3.6. Surface atomic structure analysis of $\text{Co}_3\text{O}_4$ samples

The crystal structures and the atom arrangements of different crystal planes of  $\text{Co}_3\text{O}_4$  samples were analyzed to figure out the structure-activity relationship and water oxidation mechanism of  $\text{Co}_3\text{O}_4$  samples. Fig. 7a is the unit-cell structure of spinel  $\text{Co}_3\text{O}_4$ . In Fig. 7b–d, the topmost surface layer atoms and the first sub-layer atoms of  $\text{Co}_3\text{O}_4$  100 and 112 and only the topmost surface layer atoms of  $\text{Co}_3\text{O}_4$  110 are exposed to the environment with dangling bonds. These atoms can be directly involved in the water oxidation reaction.

As shown in Fig. 7, there are numerous types of active sites for water oxidation reaction [29,44–47], one of which is a single active site of  $\text{Co}^{2+}_{\text{Td}}$  or  $\text{Co}^{3+}_{\text{Oh}}$ . It is easy to find that all the surfaces of three  $\text{Co}_3\text{O}_4$  (100,

110 and 112) contain active site of single  $\text{Co}^{2+}_{\text{Td}}$  or single  $\text{Co}^{3+}_{\text{Oh}}$ . If the oxygen is generated primarily at the single active site, the three catalysts will show similar catalytic performance, and it is contrary to our experimental results. Actually, dual-Co in spinel  $\text{Co}_3\text{O}_4$  is a better active site than single-Co for catalyzing water oxidation, which have been confirmed by time-resolved FT-IR spectroscopy and quantum chemical calculation in previous reports [29,47]. In Fig. 7, all the samples' surfaces have the same dual-Co sites of  $\text{Co}^{3+}_{\text{Oh}}-\text{Co}^{3+}_{\text{Oh}}$ ,  $\text{Co}^{2+}_{\text{Td}}-\text{Co}^{3+}_{\text{Oh}}$  and  $\text{Co}^{2+}_{\text{Td}}-\text{Co}^{2+}_{\text{Td}}$  with the ionic distance of  $2.854 \text{ \AA}$ ,  $3.346 \text{ \AA}$  and  $5.708 \text{ \AA}$ , respectively. However, a unique  $\text{Co}^{2+}_{\text{Td}}-\text{Co}^{2+}_{\text{Td}}$  site with the ionic distance of  $3.495 \text{ \AA}$  only exists in {110} and {112}. This structural difference between {100} and {110}/{112} may significantly influence their water oxidation activity and the detailed discussion is shown as follows.

Firstly, above photocatalytic water oxidation results have been confirmed experimentally that the  $\text{Co}^{2+}_{\text{Td}}$  ions in  $\text{Co}_3\text{O}_4$  are the main active species for water oxidation. In addition, another dual-Co active site of  $\text{Co}^{3+}_{\text{Oh}}-\text{Co}^{3+}_{\text{Oh}}$  is existed in the surface of all samples, so it has relatively small influence on the activity difference among three  $\text{Co}_3\text{O}_4$  samples. Therefore, we mainly focus on dual-Co active sites related with  $\text{Co}^{2+}_{\text{Td}}$  ions. Secondly, although the  $\text{Co}^{2+}_{\text{Td}}-\text{Co}^{3+}_{\text{Oh}}$  sites with ionic distance of  $3.346 \text{ \AA}$  may be potential dual-Co active sites, these dual-Co active sites have relatively small impact on the activity difference because all three crystal planes ({112}, {110} and {100}) possess these  $\text{Co}^{2+}_{\text{Td}}-\text{Co}^{3+}_{\text{Oh}}$  sites. Thirdly, the  $\text{Co}^{2+}_{\text{Td}}-\text{Co}^{2+}_{\text{Td}}$  sites ( $3.495 \text{ \AA}$ ) have been confirmed as excellent adsorption sites for water oxidation (the O–O bond forms on a single active site) [45]. In a theoretical water oxidation mechanism which water is adsorb preferentially at bridge sites between either two  $\text{Co}^{2+}_{\text{Td}}$  or two  $\text{Co}^{3+}_{\text{Oh}}$  ions on  $\text{Co}_3\text{O}_4$  {110}, water oxidation on  $\text{Co}^{2+}_{\text{Td}}$  ions show a smaller overpotential ( $0.46 \text{ V}$ ) than that on  $\text{Co}^{3+}_{\text{Oh}}$  ions ( $0.66 \text{ V}$ ) at a water coverage of 25% [45]. Furthermore, the  $\text{Co}^{2+}_{\text{Td}}-\text{Co}^{2+}_{\text{Td}}$  sites ( $3.495 \text{ \AA}$ ) can act as dual-Co active sites for the O–O bond formation between two  $\text{Co}^{2+}_{\text{Td}}$  ions because of the appropriate ionic distance for O–O bond formation (the bond length of O–O bond is ca.  $1.405 \text{ \AA}$  [48,49]). That is, water attack in two  $\text{Co}_{\text{Td}}=\text{O}$  catalytic centers ( $\text{Co}_{\text{Td}}-\text{O}-\text{H}-\text{O}(\text{H})-\text{O}-\text{Co}_{\text{Td}}$ ) and/or Oxo-Coupling ( $\text{Co}_{\text{Td}}-\text{O}-\text{O}-\text{Co}_{\text{Td}}$ ) (Scheme S1) [48–50].

A high-efficient (comparable with PS II) Ru based molecular catalyst documented shows a synergistic two molecules catalysis mechanism that the O–O bond forms between two Ru ions with a distance between two molecules closed to  $3.495 \text{ \AA}$  [51]. Furthermore, the faster O–O bond formation process in  $\text{Co}^{2+}_{\text{Td}}-\text{Co}^{2+}_{\text{Td}}$  sites ( $3.495 \text{ \AA}$ ) may cause a poorer oxygen reduction reaction activity of {110}/{112} facets than that of {100} facets. The oxygen reduction reaction (forming water) is

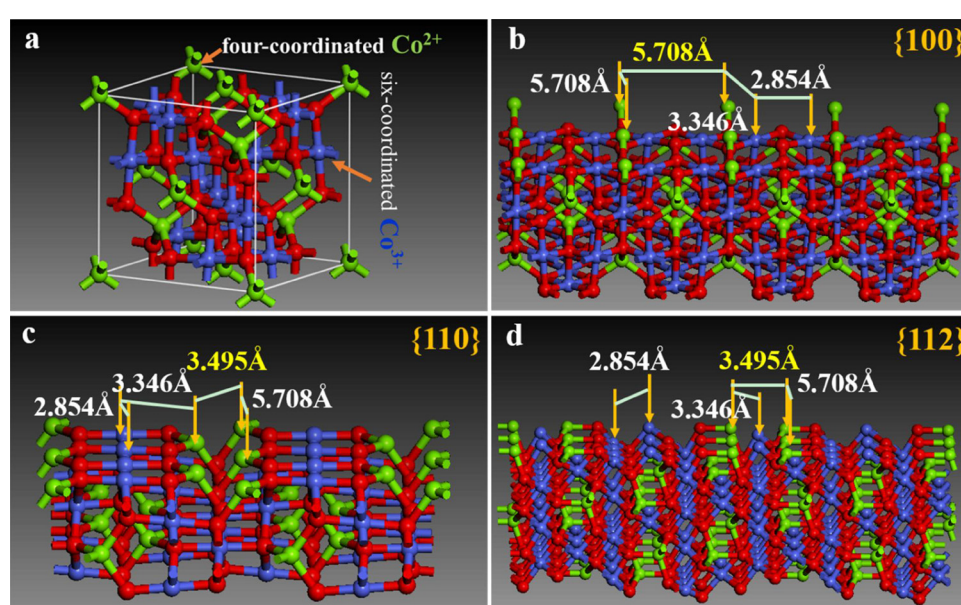


Fig. 7. (a) The unit cell structure of spinel  $\text{Co}_3\text{O}_4$ , green ball is  $\text{Co}^{2+}$ , blue ball denotes  $\text{Co}^{3+}$  and red ball is  $\text{O}^{2-}$ . The crystal structure model and surface atoms arrangement of  $\text{Co}_3\text{O}_4$  with different exposed facets for (b) {100}, (c) {110} and (d) {112}. The  $\text{Co}_3\text{O}_4$  structure model is obtained from inorganic crystal structure database (ICSD) with the corresponding JCPDS file (For interpretation of the references to colour in this figure legend, the reader is referred to the web version of this article).

the reverse reaction of water oxidation and always undergoes the break of the O–O bonds of oxygen. Previous study [20] reveals that {100} facets of  $\text{Co}_3\text{O}_4$  nanocrystal shows better activity than {110} facets for catalyzing oxygen reduction reaction (ORR), which is consistent with our deduction.

It is worth noting that the  $\text{Co}_{\text{Td}}^{2+}$ - $\text{Co}_{\text{Td}}^{2+}$  sites with distance of 3.495 Å only exist in the bulk of  $\text{Co}_3\text{O}_4$  100 are not considered as active dual-Co sites. As shown in Scheme S2, one of the  $\text{Co}_{\text{Td}}^{2+}$  ions ( $\text{Co}^{2+}$ -2) is located at the third sublayer and in a four-coordinated pattern without dangling bonds as the most bulk  $\text{Co}^{2+}$  ions. Thus, it is proposed that these  $\text{Co}_{\text{Td}}^{2+}$ - $\text{Co}_{\text{Td}}^{2+}$  sites are difficult to synergistically catalyze water oxidation. The  $\text{Co}_{\text{Td}}^{2+}$ - $\text{Co}_{\text{Td}}^{2+}$  sites with ionic distance of 5.708 Å are too long for synergistically form O–O bonds with bond length of ca. 1.405 Å (the bond length of Co-O bond is ca. 1.943 Å), resulting in difficultly synergistic catalysis. Therefore, we propose that the possession of the unique  $\text{Co}_{\text{Td}}^{2+}$ - $\text{Co}_{\text{Td}}^{2+}$  sites (3.495 Å) causes the better water oxidation activities for  $\text{Co}_3\text{O}_4$  112 and 110. This  $\text{Co}_{\text{Td}}^{2+}$ - $\text{Co}_{\text{Td}}^{2+}$  sites (3.495 Å) are expected as superior active sites because the obviously higher activities of  $\text{Co}_3\text{O}_4$  110 and 112 compared with that of  $\text{Co}_3\text{O}_4$  100. In addition, relatively larger surface energy of  $\text{Co}_3\text{O}_4$  112 (1.46 J/m<sup>2</sup>) and  $\text{Co}_3\text{O}_4$  110 (1.31 J/m<sup>2</sup>) compared with that of  $\text{Co}_3\text{O}_4$  100 (0.92 J/m<sup>2</sup>) may also account for the relatively better activity of the former two catalysts in thermodynamics [52].

Other morphological effects like the corners and edges effect have relatively minor impact on the activities of different  $\text{Co}_3\text{O}_4$  samples, which can be confirmed by the similar catalytic activities between  $\text{Co}_3\text{O}_4$  110 and 112. Hence, the primary influencing factor of water oxidation activity of different well-defined  $\text{Co}_3\text{O}_4$  crystals should be the different surface atoms constitutions and the corresponding different catalytically active sites.

#### 4. Conclusion

In summary, facet effect of  $\text{Co}_3\text{O}_4$  nanocrystals on visible-light driven water oxidation is investigated using model catalysts of  $\text{Co}_3\text{O}_4$  nanocubes, nanorods and nanosheets with primarily exposed crystal planes of {100}, {110} and {112}, respectively. Using time-resolve laser flash photolysis technology, the facet-dependent water oxidation activities of model  $\text{Co}_3\text{O}_4$  catalysts are distinguished in nanosecond scale. {110} and {112} planes always exhibit similar catalytic performance for water oxidation and their activities are clearly better than that of {100} planes. Based on the surface structure analysis in atomic/ionic level, we discover that an active  $\text{Co}_{\text{Td}}^{2+}$ - $\text{Co}_{\text{Td}}^{2+}$  sites with an ionic distance of 3.495 Å that exist merely in the interfaces of unit-cells of {110} and {112} planes. The presence of the superior  $\text{Co}_{\text{Td}}^{2+}$ - $\text{Co}_{\text{Td}}^{2+}$  sites with an ionic distance of 3.495 Å in {110} and {112} planes should be responsible for their better activities of  $\text{Co}_3\text{O}_4$  nanorods and nanosheets. Moreover, the four-coordinated  $\text{Co}_{\text{Td}}^{2+}$  ions in spinel  $\text{Co}_3\text{O}_4$  are proved experimentally to be more active than six-coordinated  $\text{Co}_{\text{Oh}}^{3+}$  ions under visible-light driven water oxidation. These results and understanding clarify the importance of atomic arrangement of surface of catalysts for water oxidation and may bring new path for exploiting heterogeneous catalysts with high-efficiency for visible-light driven water oxidation.

#### Conflict of interest

The authors declare no competing financial interest.

#### Acknowledgments

This work was financially supported by the National Natural Science Foundation of China (Grants No. 21773096), Fundamental Research Funds for the Central Universities (lzujbky-2018-k08), the Natural Science Foundation of Gansu Province (17JR5RA186) and the Open Funds of the State Key Laboratory of Rare Earth Resource Utilization

(RERU2017001).

#### Appendix A. Supplementary data

Supplementary material related to this article can be found, in the online version, at doi:<https://doi.org/10.1016/j.apcatb.2018.05.067>.

#### References

- [1] N.S. Lewis, D.G. Nocera, Powering the planet: chemical challenges in solar energy utilization, *Proc. Natl. Acad. Sci. U. S. A.* 103 (2006) 15729–15735.
- [2] D. Gust, T.A. Moore, A.L. Moore, Solar fuels via artificial photosynthesis, *Acc. Chem. Res.* 42 (2009) 1890–1898.
- [3] M.W. Kanan, D.G. Nocera, In situ formation of an oxygen-evolving catalyst in neutral water containing phosphate and  $\text{Co}^{2+}$ , *Science* 321 (2008) 1072–1075.
- [4] J. Huang, Y. Zhang, Y. Ding, Rationally designed/constructed  $\text{Co}_3\text{O}_4/\text{WO}_3$  anode for efficient photoelectrochemical water oxidation, *ACS Catal.* 7 (2017) 1841–1845.
- [5] M. Zheng, Y. Ding, L. Yu, X. Du, Y. Zhao, In situ grown pristine cobalt sulfide as bifunctional photocatalyst for hydrogen and oxygen evolution, *Adv. Funct. Mater.* (2017) 1605846-n/a.
- [6] B.M. Hunter, H.B. Gray, A.M. Müller, Earth-abundant heterogeneous Water oxidation catalysts, *Chem. Rev.* 116 (2016) 14120–14136.
- [7] H. Liu, R. Moré, H. Grundmann, C. Cui, R. Erni, G.R. Patzke, Promoting photochemical water oxidation with metallic band structures, *J. Am. Chem. Soc.* 138 (2016) 1527–1535.
- [8] G.P. Gardner, Y.B. Go, D.M. Robinson, P.F. Smith, J. Hadermann, A. Abakumov, M. Greenblatt, G.C. Dismukes, Structural requirements in lithium cobalt oxides for the catalytic oxidation of water, *Angew. Chem. Int. Ed.* 51 (2012) 1616–1619.
- [9] Y. Zhang, J. Huang, Y. Ding, Porous  $\text{Co}_3\text{O}_4/\text{CuO}$  hollow polyhedral nanocages derived from metal-organic frameworks with heterojunctions as efficient photocatalytic water oxidation catalysts, *Appl. Catal. B Environ.* 198 (2016) 447–456.
- [10] C.J. Gagliardi, A.K. Vannucci, J.J. Concepcion, Z. Chen, T.J. Meyer, The role of proton coupled electron transfer in water oxidation, *Energy Environ. Sci.* 5 (2012) 7704–7717.
- [11] N.-T. Suen, S.-F. Hung, Q. Quan, N. Zhang, Y.-J. Xu, H.M. Chen, Electrocatalysis for the oxygen evolution reaction: recent development and future perspectives, *Chem. Soc. Rev.* 46 (2017) 337–365.
- [12] L. Hu, Q. Peng, Y. Li, Selective synthesis of  $\text{Co}_3\text{O}_4$  nanocrystal with different shape and crystal plane effect on catalytic property for methane combustion, *J. Am. Chem. Soc.* 130 (2008) 16136–16137.
- [13] K. Zhou, Y. Li, Catalysis based on nanocrystals with well-defined facets, *Angew. Chem. Int. Ed.* 51 (2012) 602–613.
- [14] X. Xie, Y. Li, Z.-Q. Liu, M. Haruta, W. Shen, Low-temperature oxidation of CO catalysed by  $\text{Co}_3\text{O}_4$  nanorods, *Nature* 458 (2009) 746–749.
- [15] F. Zaera, Nanostructured materials for applications in heterogeneous catalysis, *Chem. Soc. Rev.* 42 (2013) 2746–2762.
- [16] J. Rosen, G.S. Hutchings, F. Jiao, Synthesis, structure, and photocatalytic properties of ordered mesoporous metal-doped  $\text{Co}_3\text{O}_4$ , *J. Catal.* 310 (2014) 2–9.
- [17] M. Suga, F. Akitा, K. Hirata, G. Ueno, H. Murakami, Y. Nakajima, T. Shimizu, K. Yamashita, M. Yamamoto, H. Ago, J.-R. Shen, Native structure of photosystem II at 1.95 Å resolution viewed by femtosecond X-ray pulses, *Nature* 517 (2015) 99–103.
- [18] F. Wen, C. Li, Hybrid artificial photosynthetic systems comprising semiconductors as light harvesters and biomimetic complexes as molecular cocatalysts, *Acc. Chem. Res.* 46 (2013) 2355–2364.
- [19] C. Zhang, C. Chen, H. Dong, J.-R. Shen, H. Dau, J. Zhao, A synthetic  $\text{Mn}_4\text{Ca}$ -cluster mimicking the oxygen-evolving center of photosynthesis, *Science* 348 (2015) 690–693.
- [20] J. Xiao, Q. Kuang, S. Yang, F. Xiao, S. Wang, L. Guo, Surface structure dependent electrocatalytic activity of  $\text{Co}_3\text{O}_4$  anchored on graphene sheets toward oxygen reduction reaction, *Sci. Rep.* 3 (2013) 2300.
- [21] Z. Chen, C.X. Kronawitter, B.E. Koel, Facet-dependent activity and stability of  $\text{Co}_3\text{O}_4$  nanocrystals towards the oxygen evolution reaction, *Phys. Chem. Chem. Phys.* 17 (2015) 29387–29393.
- [22] Y. Zhang, F. Ding, C. Deng, S. Zhen, X. Li, Y. Xue, Y.-M. Yan, K. Sun, Crystal plane-dependent electrocatalytic activity of  $\text{Co}_3\text{O}_4$  toward oxygen evolution reaction, *Catal. Commun.* 67 (2015) 78–82.
- [23] J. Feng, H.C. Zeng, Size-controlled growth of  $\text{Co}_3\text{O}_4$  nanocubes, *Chem. Mater.* 15 (2003) 2829–2835.
- [24] S.W. Hwang, A. Umar, S.H. Kim, S.A. Al-Sayari, M. Abaker, A. Al-Hajry, A.M. Stephan, Low-temperature growth of well-crystalline  $\text{Co}_3\text{O}_4$  hexagonal nanodisks as anode material for lithium-ion batteries, *Electrochim. Acta* 56 (2011) 8534–8538.
- [25] X. Zhou, J. Huang, F. Zhang, Y. Zhao, Y. Zhang, Y. Ding, Iron-cobalt bimetal oxide nanorods as efficient and robust water oxidation catalysts, *Dalton Trans.* 46 (2017) 10602–10610.
- [26] H.-Y. Wang, S.-F. Hung, H.-Y. Chen, T.-S. Chan, H.M. Chen, B. Liu, In operando identification of geometrical-site-dependent water oxidation activity of spinel  $\text{Co}_3\text{O}_4$ , *J. Am. Chem. Soc.* 138 (2016) 36–39.
- [27] J.-X. Jian, C. Ye, X.-Z. Wang, M. Wen, Z.-J. Li, X.-B. Li, B. Chen, C.-H. Tung, L.-Z. Wu, Comparison of  $\text{H}_2$  photogeneration by [FeFe]-hydrogenase mimics with CdSe QDs and Ru(bpy)<sub>3</sub>Cl<sub>2</sub> in aqueous solution, *Energy Environ. Sci.* 9 (2016) 2083–2089.

- [28] P.W. Menezes, A. Indra, D. González-Flores, N.R. Sahraie, I. Zaharieva, M. Schwarze, P. Strasser, H. Dau, M. Driess, High-performance oxygen redox catalysis with multifunctional cobalt oxide nanochains: morphology-dependent activity, *ACS Catal.* 5 (2015) 2017–2027.
- [29] M. Zhang, M. de Respinis, H. Frei, Time-resolved observations of water oxidation intermediates on a cobalt oxide nanoparticle catalyst, *Nat. Chem.* 6 (2014) 362–367.
- [30] F. Song, Y. Ding, B. Ma, C. Wang, Q. Wang, X. Du, S. Fu, J. Song,  $K_7[\text{CoIII}(\text{CoII})(\text{H}_2\text{O})\text{W}_{11}\text{O}_{39}]$ : a molecular mixed-valence keggin polyoxometalate catalyst of high stability and efficiency for visible light-driven water oxidation, *Energy Environ. Sci.* 6 (2013) 1170–1184.
- [31] J. Wei, Y. Feng, P. Zhou, Y. Liu, J. Xu, R. Xiang, Y. Ding, C. Zhao, L. Fan, C. Hu, A bioinspired molecular polyoxometalate catalyst with two cobalt(II) oxide cores for photocatalytic water oxidation, *ChemSusChem* 8 (2015) 2630–2634.
- [32] Á. Valdés, G.J. Kroes, Cluster study of the photo-oxidation of water on rutile titanium dioxide ( $\text{TiO}_2$ ), *J. Phys. Chem. C* 114 (2010) 1701–1708.
- [33] J. Chen, Y.-F. Li, P. Sit, A. Selloni, Chemical dynamics of the first proton-coupled electron transfer of water oxidation on  $\text{TiO}_2$  anatase, *J. Am. Chem. Soc.* 135 (2013) 18774–18777.
- [34] Z. Huang, Y.V. Geletii, D.G. Musaev, C.L. Hill, T. Lian, Spectroscopic studies of light-driven water oxidation catalyzed by polyoxometalates, *Ind. Eng. Chem. Res.* 51 (2012) 11850–11859.
- [35] H. Lindström, S. Södergren, A. Solbrand, H. Rensmo, J. Hjelm, A. Hagfeldt, S.-E. Lindquist,  $\text{Li}^+$  ion insertion in  $\text{TiO}_2$  (anatase). 2. Voltammetry on nanoporous films, *J. Phys. Chem. B* 101 (1997) 7717–7722.
- [36] Y. Zhang, X. Zhou, F. Zhang, T. Tian, Y. Ding, H. Gao, Design and synthesis of Cu modified cobalt oxides with hollow polyhedral nanocages as efficient electrocatalytic and photocatalytic water oxidation catalysts, *J. Catal.* 352 (2017) 246–255.
- [37] H.B. Tao, L. Fang, J. Chen, H.B. Yang, J. Gao, J. Miao, S. Chen, B. Liu, Identification of surface reactivity descriptor for transition metal oxides in oxygen evolution reaction, *J. Am. Chem. Soc.* 138 (2016) 9978–9985.
- [38] H. Li, J. Shang, H. Zhu, Z. Yang, Z. Ai, L. Zhang, Oxygen vacancy structure associated photocatalytic water oxidation of  $\text{BiOCl}$ , *ACS Catal.* 6 (2016) 8276–8285.
- [39] Z.-Q. Liu, H. Cheng, N. Li, T.Y. Ma, Y.-Z. Su,  $\text{ZnCo}_2\text{O}_4$  quantum dots anchored on nitrogen-doped carbon nanotubes as reversible oxygen reduction/evolution electrocatalysts, *Adv. Mater.* 28 (2016) 3777–3784.
- [40] J. Merikhi, H.-O. Jungk, C. Feldmann, Sub-micrometer  $\text{CoAl}_2\text{O}_4$  pigment particles – synthesis and preparation of coatings, *J. Mater. Chem.* 10 (2000) 1311–1314.
- [41] M.C. Biesinger, B.P. Payne, A.P. Grosvenor, L.W.M. Lau, A.R. Gerson, R.S.C. Smart, Resolving surface chemical states in XPS analysis of first row transition metals, oxides and hydroxides: Cr, Mn, Fe, Co and Ni, *Appl. Surf. Sci.* 257 (2011) 2717–2730.
- [42] X. Duan, M. Pan, F. Yu, D. Yuan, Synthesis, structure and optical properties of  $\text{CoAl}_2\text{O}_4$  spinel nanocrystals, *J. Alloys Compd.* 509 (2011) 1079–1083.
- [43] A.J.C. Mary, A.C. Bose, Hydrothermal synthesis of Mn-doped  $\text{ZnCo}_2\text{O}_4$  electrode material for high-performance supercapacitor, *Appl. Surf. Sci.* 425 (2017) 201–211.
- [44] J. Rosen, G.S. Hutchings, F. Jiao, Ordered mesoporous cobalt oxide as highly efficient oxygen evolution catalyst, *J. Am. Chem. Soc.* 135 (2013) 4516–4521.
- [45] J. Chen, A. Selloni, Water adsorption and oxidation at the  $\text{Co}_3\text{O}_4$  (110) surface, *J. Phys. Chem. Lett.* 3 (2012) 2808–2814.
- [46] L.-P. Wang, T. Van Voorhis, Direct-coupling  $\text{O}_2$  bond forming a pathway in cobalt oxide water oxidation catalysts, *J. Phys. Chem. Lett.* 2 (2011) 2200–2204.
- [47] C.P. Plaisance, R.A. van Santen, Structure sensitivity of the oxygen evolution reaction catalyzed by cobalt(II,III) oxide, *J. Am. Chem. Soc.* 137 (2015) 14660–14672.
- [48] J.-W. Wang, P. Sahoo, T.-B. Lu, Reinvestigation of water oxidation catalyzed by a dinuclear cobalt polypyridine complex: identification of  $\text{CoO}_x$  as a real heterogeneous catalyst, *ACS Catal.* 6 (2016) 5062–5068.
- [49] M. Okamura, M. Kondo, R. Kuga, Y. Kurashige, T. Yanai, S. Hayami, V.K.K. Praneeth, M. Yoshida, K. Yoneda, S. Kawata, S. Masaoka, A pentanuclear iron catalyst designed for water oxidation, *Nature* 530 (2016) 465–468.
- [50] T. Ishizuka, A. Watanabe, H. Kotani, D. Hong, K. Satonaka, T. Wada, Y. Shiota, K. Yoshizawa, K. Ohara, K. Yamaguchi, S. Kato, S. Fukuzumi, T. Kojima, Homogeneous photocatalytic water oxidation with a dinuclear  $\text{Co}^{II}$ -pyridylmethylamine complex, *Inorg. Chem.* 55 (2016) 1154–1164.
- [51] L. Duan, F. Bozoglian, S. Mandal, B. Stewart, T. Privalov, A. Llobet, L. Sun, A molecular ruthenium catalyst with water-oxidation activity comparable to that of photosystem II, *Nat. Chem.* 4 (2012) 418–423.
- [52] D. Su, S. Dou, G. Wang, Single crystalline  $\text{Co}_3\text{O}_4$  nanocrystals exposed with different crystal planes for  $\text{Li}-\text{O}_2$  batteries, *Sci. Rep.* 4 (2014) 5767.